

# SCIENTIFIC REPORTS



OPEN

## Depth-specific optogenetic control *in vivo* with a scalable, high-density $\mu$ LED neural probe

Robert Scharf<sup>1</sup>, Tomomi Tsunematsu<sup>2</sup>, Niall McAlinden<sup>1</sup>, Martin D. Dawson<sup>1</sup>, Shuzo Sakata<sup>2</sup> & Keith Mathieson<sup>1</sup>

Received: 13 January 2016

Accepted: 03 June 2016

Published: 23 June 2016

Controlling neural circuits is a powerful approach to uncover a causal link between neural activity and behaviour. Optogenetics has been widely adopted by the neuroscience community as it offers cell-type-specific perturbation with millisecond precision. However, these studies require light delivery in complex patterns with cellular-scale resolution, while covering a large volume of tissue at depth *in vivo*. Here we describe a novel high-density silicon-based microscale light-emitting diode ( $\mu$ LED) array, consisting of up to ninety-six 25  $\mu$ m-diameter  $\mu$ LEDs emitting at a wavelength of 450 nm with a peak irradiance of 400 mW/mm<sup>2</sup>. A width of 100  $\mu$ m, tapering to a 1  $\mu$ m point, and a 40  $\mu$ m thickness help minimise tissue damage during insertion. Thermal properties permit a set of optogenetic operating regimes, with  $\sim$ 0.5  $^{\circ}$ C average temperature increase. We demonstrate depth-dependent activation of mouse neocortical neurons *in vivo*, offering an inexpensive novel tool for the precise manipulation of neural activity.

With the advent of optogenetics<sup>1–3</sup> it is now possible to directly activate and inhibit neural activity with genetic specificity<sup>4–6</sup>. This is allowing the precise manipulation of neural circuits, giving insight into neural coding and furthering the understanding of how neural activity links to behavioural responses. However, in order to fully exploit this technique, light needs to be delivered at high spatiotemporal resolution to regions that are often deep within the brain, necessitating the development of novel photonic technologies. The conventional approach for light delivery in the brain is to use an optic fibre<sup>7,8</sup>, which can control neural activity in a cell-type-specific manner with high temporal resolution in regions where opsins have been expressed<sup>4–6</sup>. However, it is challenging to deliver light through a fibre at high spatial resolution. This is particularly acute when a specific cell type is distributed across functionally distinct sub-regions at the sub-millimetre scale, such as cortical GABAergic neurons. Improvements in spatial resolution have primarily been realised through multiphoton stimulation, which has demonstrated sub-cellular resolution<sup>9–12</sup>. However, because of light absorption and scattering in the brain, it is difficult for these approaches to manipulate neural activity beyond 1 mm. Penetrating arrays offer a solution by moving the light source into the brain. Here we demonstrate *in vivo*, multi-point optical stimulation at resolutions approaching the cellular scale, and covering the full depth of the mouse neocortex. This technique can be extended to allow light delivery many millimetres into the brain.

Other groups have pursued related approaches. In particular, multipoint-emitting optic fibres<sup>13,14</sup> have been employed, as have monolithically integrated dielectric waveguides<sup>15</sup> and three-dimensional multi-waveguide probes<sup>16</sup>. These are promising approaches that have demonstrated the benefits of spatiotemporal optogenetics at depth. However, they employ expensive and bulky light sources where the complexity of the optical setup becomes an issue as they are scaled up to multiple stimulation sites. To address this scalability issue, an alternative approach is to have light sources integrated onto the probe and capable of being inserted into the brain. Microscale light-emitting diodes ( $\mu$ LEDs) offer such a solution<sup>17–20</sup>. A multimodal implant has been developed with four connected  $\mu$ LEDs<sup>17</sup>. However, it is still challenging to induce rich spatiotemporal patterns of population activity at depth *in vivo*. We previously demonstrated an individually addressable, sapphire-based  $\mu$ LED probe<sup>18</sup> and showed activation of neurons *in vivo*<sup>20</sup>. However, the problem with this approach is that the sapphire substrate cannot be reliably thinned beyond 100  $\mu$ m making the probe invasive and susceptible to inducing damage

<sup>1</sup>Institute of Photonics, Dept. of Physics, SUPA, University of Strathclyde, Glasgow G1 1RD, UK. <sup>2</sup>Strathclyde Institute of Pharmacy and Biomedical Sciences, University of Strathclyde, Glasgow G4 0RE, UK. Correspondence and requests for materials should be addressed to S.S. (email: shuzo.sakata@strath.ac.uk) or K.M. (email: keith.mathieson@strath.ac.uk)

in the surrounding neural tissue. Recent work has demonstrated optical stimulation of discrete neurons using a four shank probe with three  $\mu$ LEDs per shank that is integrated with recording electrodes<sup>21</sup>. The  $\mu$ LEDs cover 150  $\mu$ m per shank and demonstrate low-level illumination is able to activate hippocampal neurons in freely moving mice. However, the full scalability of this approach has not been demonstrated yet.

Here we report on a device that uses  $\mu$ LEDs on a silicon substrate that allows complete depth coverage of the mouse cortex at high spatial resolution. This neural probe has up to 96 independent optical sites and is capable of inducing rich spatiotemporal patterns of neural activity in the brain. The advanced microfabrication techniques available for silicon devices open up a wide variety of processes that permit probes that measure 40  $\mu$ m in thickness and have 25  $\mu$ m-diameter  $\mu$ LEDs spaced at 50  $\mu$ m. These  $\mu$ LEDs are easily controlled using readily available integrated circuits, creating an inexpensive miniature system to control neurons *in vivo*. The integration of electrically-driven light sources on to neural probes makes this approach scalable to 100 s of sites and beyond. However, there are drawbacks around the light emission profile and power dissipation of devices such as this. Here we show that with the correct design criteria, each  $\mu$ LED has a dynamic range that extends from individual neurons to 1000 s and that the thermal properties of the silicon/tissue interface mean that pulse widths and repetition rates can be realised that are well suited to optogenetic activation. Using this  $\mu$ LED probe, we demonstrate depth-specific optogenetic neural activations in the mouse neocortex *in vivo*. Specifically, we show the feasibility of two novel optogenetic experiments, which have been challenging with conventional approaches: depth-specific activations of cortical GABAergic interneurons and the induction of various spatiotemporal patterns of neural population activity even with a simple pan-neuronal expression of opsins in the cortex.

**A novel neural probe for multi-site light delivery.** In order to produce this implantable, high-resolution device, we employed semiconductor microfabrication techniques and used GaN-on-silicon wafer technology (Supplementary Figure S1). The silicon substrate enables final devices that have sixteen 25  $\mu$ m-diameter  $\mu$ LEDs (Fig. 1a,b) in a compact design of 100  $\mu$ m  $\times$  40  $\mu$ m  $\times$  3 mm. The  $\mu$ LEDs are produced in GaN layers, which include quantum well structures to enhance radiative recombination (see Methods). Each  $\mu$ LED is capable of producing surface irradiance of  $\sim$ 400 mW/mm<sup>2</sup> at 5 mA current (Fig. 1c,d). When activating neurons using optogenetics, it is important to consider not only the spatial separation of the light sources, but also how light propagates through brain tissue from the  $\mu$ LED surface. The Lambertian emission profile of photons from this surface can be seen experimentally in Fig. 1e for the probes in fluorescein solution. This data was used to verify a Monte Carlo model (see Methods), which then allowed the study of light propagation in brain tissue (Fig. 1f). A threshold for optogenetic activation of 1 mW/mm<sup>2</sup> is often used, allowing an estimation of the volume of tissue affected as a function of  $\mu$ LED intensity (Fig. 1g). If the neuron density is taken as 10<sup>5</sup> neurons/mm<sup>3</sup><sup>22,23</sup>, then a rough estimate of the number of neurons affected can be calculated. This demonstrates that each  $\mu$ LED has a dynamic range that extends up to  $\sim$ 1500 at 5 mA. More neurons can be recruited at higher drive currents; however, the limiting factor becomes the dissipation of electrical power as heat at the surface of the  $\mu$ LED. This is an important factor when implanting optoelectronic devices, such as this, into the brain. Neurons are known to be very sensitive to thermal fluctuations, though exact quantitative data is varied and difficult to interpret<sup>24,25</sup>. In order to study the thermal characteristics of the system, we conducted thermal imaging measurements in air (Supplementary Figure S2), replicated the data using a COMSOL Multiphysics<sup>®</sup> model (see Methods) and used the model to predict heat dissipation from the probe in brain tissue. This model showed that most of the heat transfer occurs along the silicon shank due to the high thermal conductivity of silicon with respect to neural tissue. The effect of the silicon substrate acting as a heat sink results in the peak temperature varying with  $\mu$ LED position (Fig. 1h), due to heat flow being restricted by proximity to the probe tip. If the furthest  $\mu$ LED from the tip ( $\mu$ LED 16) is considered (cf. Supplementary Figures S3 and S4 for  $\mu$ LED 1), then at irradiance values of  $\sim$ 150 mW/mm<sup>2</sup> (1 mA drive current) the peak temperature change at the surface of the  $\mu$ LED varies from 0.4 to 4 °C dependant on pulse width. This decays with time after the pulse and distance into the brain (Fig. 1i,j). It is important to note that this is the peak temperature that occurs during operation. At this irradiance level (150 mW/mm<sup>2</sup>), the thermal characteristics of the neural probe permit duty cycles of  $\sim$ 10% without the average temperature rise extending beyond 0.5 °C (Fig. 1k). We further investigated the relationship between the size and pitch of  $\mu$ LEDs and the achievable spatial resolution of optical stimulation (Supplementary Figure S5). We found that at a  $\mu$ LED pitch of 50  $\mu$ m, 25  $\mu$ m-diameter  $\mu$ LEDs offer a resolution similar to that of smaller diameter (10  $\mu$ m)  $\mu$ LEDs, due mainly to the Lambertian emission profile of the light source.

**Depth-specific activation of cortical GABAergic neurons *in vivo*.** An advantage of this probe is that it allows us to deliver light at the scale of 10 s to 100 s of microns resolution across different depths of the brain. To demonstrate this capability, we chose the mouse neocortex, in which the six-layered structure is the most prominent anatomical feature with distinct functional properties<sup>26</sup> and the thickness of each layer is sub-millimetre with many cell types distributed across layers. In particular, we focused on a type of GABAergic neuron that is sparsely distributed across layers with recent evidence of functional variations<sup>27–29</sup>, but where it is challenging to optogenetically activate in a depth-specific manner *in vivo*.

We inserted a  $\mu$ LED probe in the urethane-anaesthetised mouse neocortex, expressing Channelrhodopsin-2 (ChR2) in parvalbumin positive (PV+) neurons (see Methods), which is a major type of cortical GABAergic interneuron<sup>30–32</sup>. To demonstrate depth specificity, we selected three  $\mu$ LED sites located at 525, 675, and 775  $\mu$ m from the probe tip. Although this probe can theoretically achieve neural control at a higher spatial resolution (Supplementary Figure S5), due to a lack of integrated electrodes, we needed to insert a recording probe nearby (several hundreds of microns). This separation required an increase in light intensity to penetrate to neurons near the recording electrodes, limiting the demonstrable resolution to 100 s of microns. As a result, we decided to sub-sample the  $\mu$ LEDs to demonstrate depth-specific activation at this scale. To evaluate effects of  $\mu$ LED stimulation on PV+ neuron activity and to compare the performance of the  $\mu$ LED probe with a conventional optic fibre approach, a silicon-based 32-channel electrode probe with an optic fibre (silicon optrode) was inserted

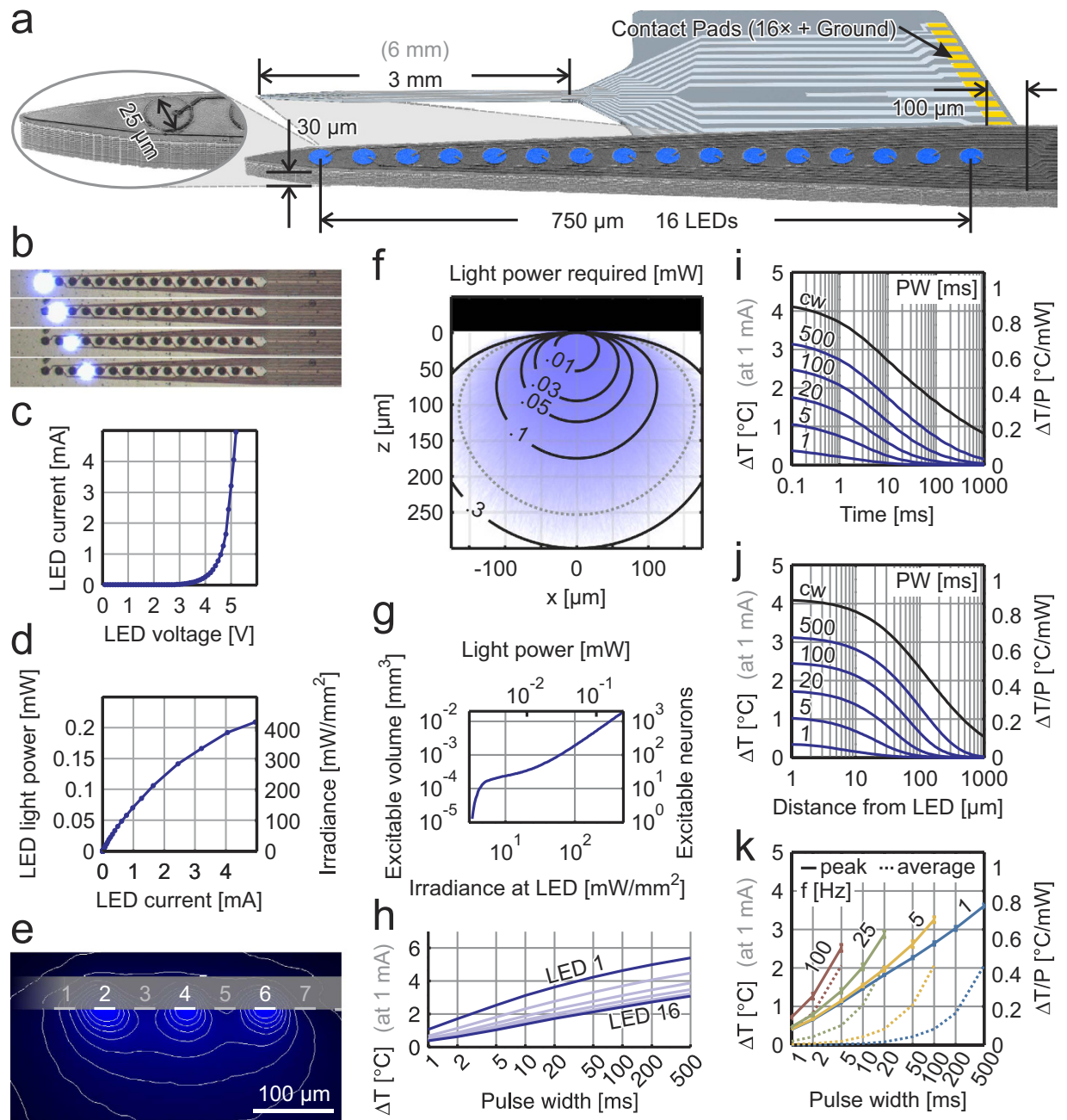


**Figure 1. Microfabrication and characterisation of a high-density silicon-based  $\mu$ LED probe.** (a) SEM image of the  $\mu$ LED probe tip (before parylene deposition, which adds  $\sim 5 \mu\text{m}$  to each side) in front of a schematic of the whole probe, 16  $\mu$ LEDs shown. (b) Operating device, single  $\mu$ LEDs turned on. (c) Current-voltage (IV) curve for a typical  $\mu$ LED. (d) Optical power output as a function of current (LI) curve for the same  $\mu$ LED. (e)  $\mu$ LED probe in fluorescein solution,  $\mu$ LEDs 2, 4 and 6 turned on simultaneously. (f) Monte Carlo simulation for light coming from one  $\mu$ LED and propagating through brain tissue, contour lines indicate light powers needed to excite ChR2 at various points (irradiance =  $1 \text{ mW}/\text{mm}^2$ ), the dotted grey contour corresponds to the maximum for the example  $\mu$ LED ( $\sim 250 \mu\text{m}$  away from the  $\mu$ LED surface at 5 mA). (g) Estimation of tissue volumes and number of neurons excitable by one  $\mu$ LED (assuming neuronal density of  $10^5 \text{ mm}^{-3}$ ). (h) Maximum temperature at various distances from the  $\mu$ LED following a pulse, temperature depends on the  $\mu$ LED position (LED 1: closest to probe tip). (i) Temperature dissipation (on surface of  $\mu$ LED 16) over time following a pulse of certain pulse width (blue) or continuously on (black). (j) Maximum temperature at various distances from  $\mu$ LED 16 following a pulse of certain pulse width (blue) or continuously on (black). (k) Peak and average temperatures of  $\mu$ LED 16 during continuous pulsed operation for various combinations of pulse width and repetition rate.

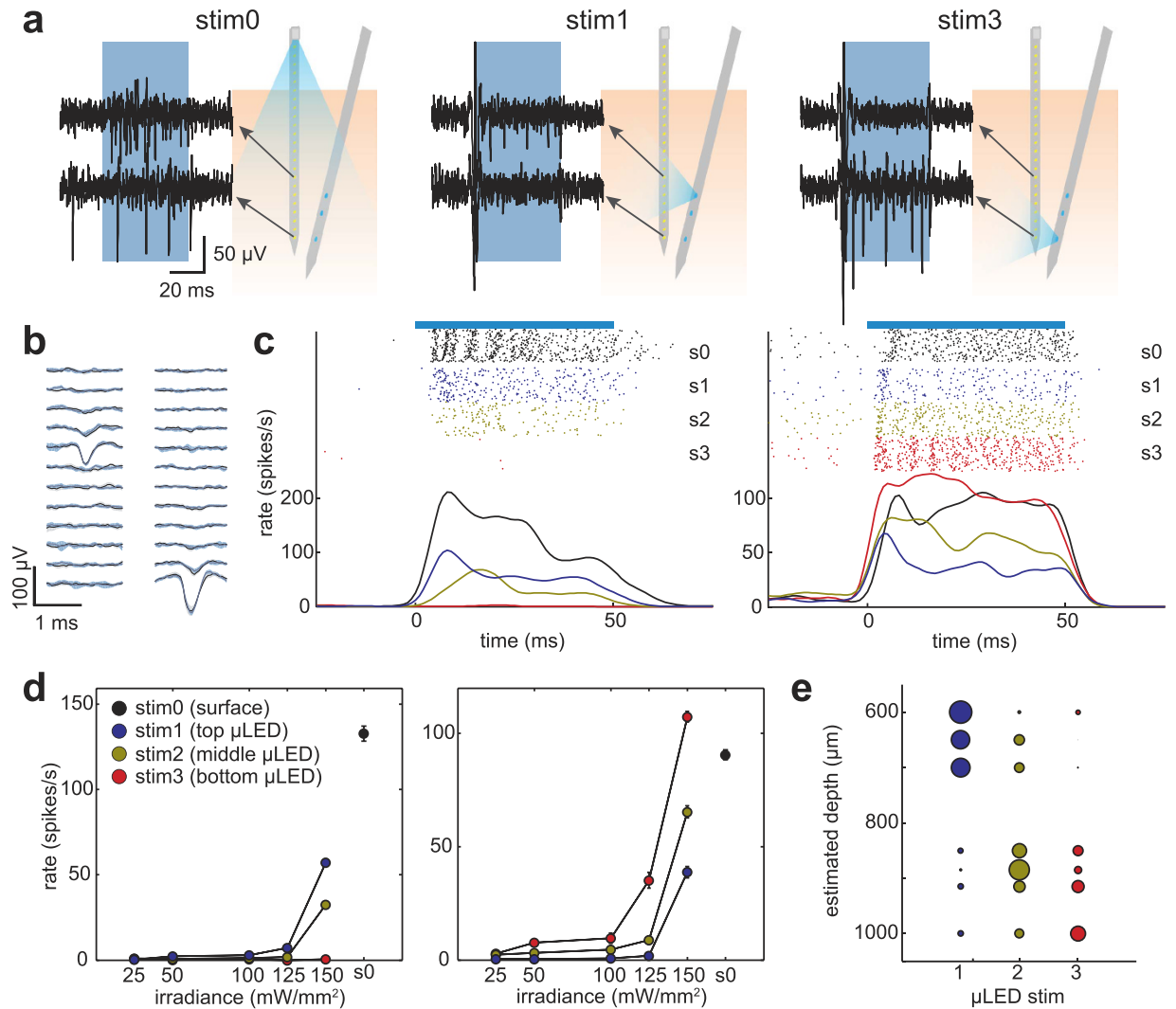


**Figure 2. Depth-dependent activation of PV+ neurons *in vivo*.** (a) Schematic of probe insertion and high-pass filtered (800 Hz) signals from two separate recording channels, which were separated by 350  $\mu\text{m}$ ; stim0: optical fibre stimulation from cortical surface (86.6  $\text{mW}/\text{mm}^2$ ), stim1 and stim3 (150  $\text{mW}/\text{mm}^2$ ): light stimulation from top and bottom  $\mu\text{LED}$ s. (b) Average spike waveforms of two exemplary PV+ cells across channels, black: spontaneous spikes, blue: optically evoked spikes, errors indicate the 95% confidence interval. (c) Peristimulus time histograms of two PV+ cells; s0: surface stimulation (stim0, 86.6  $\text{mW}/\text{mm}^2$ ), s1–3:  $\mu\text{LED}$  stimulations (stim1–3, 150  $\text{mW}/\text{mm}^2$ ); blue bar indicates light stimulus and the ticks indicate spike times across 100 trials for each stimulation case. (d) Average light evoked responses across different stimulus conditions and irradiances; effects of  $\mu\text{LED}$  stimulation sites and irradiance were highly significant in both cells (top:  $F_{2,8} = 342.5$ ,  $F_{4,8} = 1153.9$ ,  $p < 0.00001$ , bottom:  $F_{2,8} = 191.98$ ,  $F_{4,9} = 2395.2$ ,  $p < 0.0001$ , two-way ANOVA); error bars indicate SEM. (e) Depth profiles of normalized responses across simultaneously recorded PV+ cells and across stimulus conditions;  $\mu\text{LED}$  number corresponds to stimulus location (stim1–3, 150  $\text{mW}/\text{mm}^2$ ); circle size represents light evoked responses normalized by sum of responses across three conditions.

(Fig. 2 and Supplementary Figure S6). The two probes were separated by 400  $\mu\text{m}$  at the cortical surface with a 20° angle. As shown in Fig. 2a, optic fibre stimulation from the cortical surface elicited spikes in two different channels, separated by 350  $\mu\text{m}$  – suggesting different cortical layers. When light illumination (50 ms, 150  $\text{mW}/\text{mm}^2$ ) was provided by the  $\mu\text{LED}$  probe, we observed that spikes were preferentially elicited in one of those channels depending upon which  $\mu\text{LED}$  was used.

To quantify this tendency, we isolated single units and measured spike rates over 100 trials across different irradiances (25–150  $\text{mW}/\text{mm}^2$ , Fig. 2b–e). In the examples in Fig. 2b–d, two simultaneously recorded neurons were located at different cortical depths based on the position of the peak amplitude of the spike waveforms (Fig. 2b). While the surface illumination elicited robust responses in these neurons,  $\mu\text{LED}$  stimulations evoked distinct responses: deeper  $\mu\text{LED}$  stimulation (stim3) elicited larger responses in the deeper neuron, whereas upper  $\mu\text{LED}$  stimulation (stim1) evoked more spikes from the superficial neuron. We quantified this tendency across different irradiance levels, by showing statistically significant effects on spiking activity dependent on

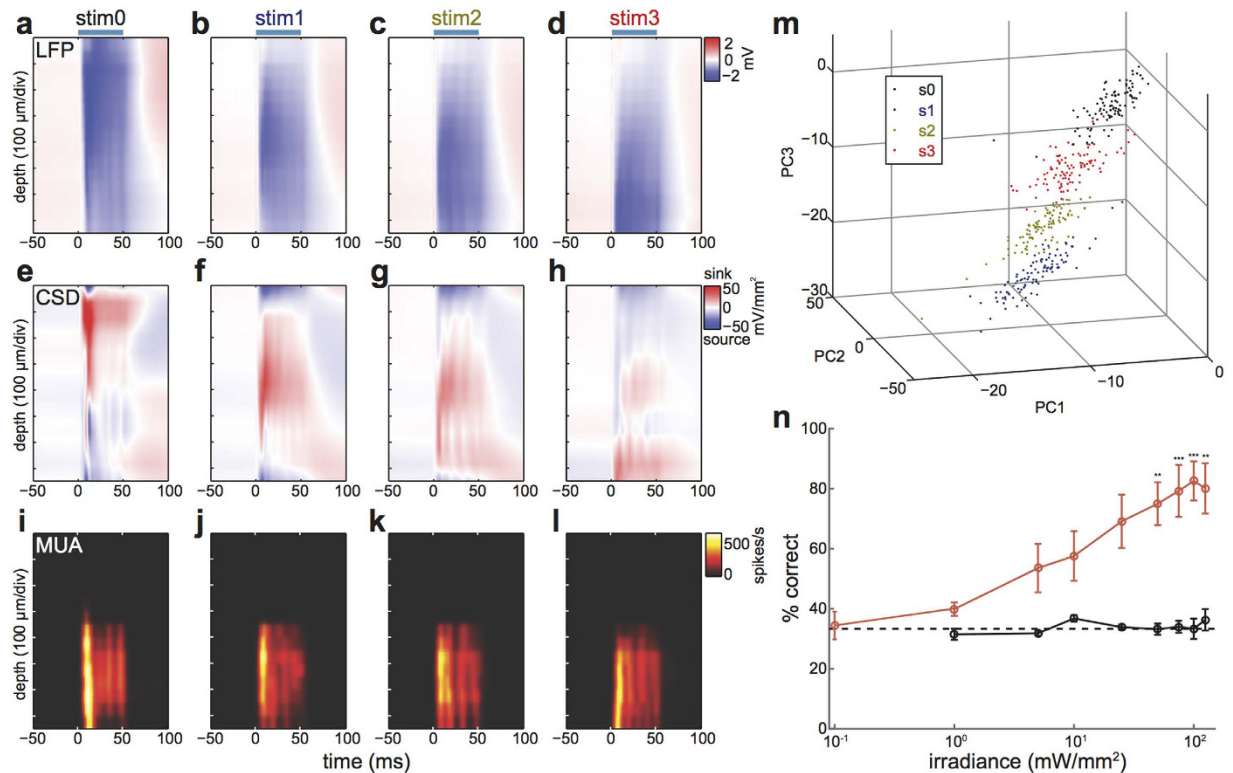


**Figure 3. Distinct spatiotemporal patterns of neural population activity induced by  $\mu$ LED stimulation *in vivo*.** (a–d) Depth profile of optically evoked local field potentials (LFPs); the average LFP ( $n = 100$ ) in each channel is shown as a function of time (light on at time  $t = 0$ , blue bars indicate light stimulus); note that the biggest deflection ( $\sim -2$  mV) was observed close to the stimulation site; stim0: optical fibre stimulation from cortical surface ( $86.6$  mW/mm $^2$ ), stim1–3: light stimulation from top, middle and bottom  $\mu$ LEDs respectively ( $150$  mW/mm $^2$ ). (e–h) Depth profile of current source density (CSD) as a function of time. (i–l) Depth profile of multiunit activities (MUA). (m) Principal component analysis (PCA) of CSD profiles; each dot represents a CSD profile for a single trial ( $n = 100$ ) and each stimulation condition. (n) Percentage of successful CSD profile classifications (after PCA) as a function of irradiance for the three  $\mu$ LED stimulations; Emx1-IRES-Cre::Ai32 shown in red ( $n = 5$ ) and Ai32 mice in black ( $n = 3$ ). Dotted line is the chance level (three  $\mu$ LEDs); error bars indicate SEM; \*\* $p < 0.005$ , \*\*\* $p < 0.001$  (two-way ANOVA with post-hoc Tukey’s honest significant difference).

stimulus location ( $p < 0.00001$ , two-way ANOVA). We further confirmed this tendency by analysing simultaneously recorded PV+ neurons ( $n = 7$ ) across layers (Fig. 2e), which showed a different magnitude of activation across PV+ neurons depending on stimulation depth. This demonstrates that  $\mu$ LED stimulation induces neural activation, at sub-millimetre resolution, across neocortical layers.

**Induction of distinct spatiotemporal population activity across cortical layers.** Another advantage of this  $\mu$ LED probe is the ability to induce distinct spatiotemporal patterns of neural population activity *in vivo*, even in the case where an animal has dense expression of ChR2 across cell populations. To demonstrate this capability, we performed a similar experiment in another transgenic line expressing ChR2 across all cortical layers (Emx1-IRES-Cre::Ai32,  $n = 5$ ) under anaesthesia, and again we compared optically evoked responses across different stimulation conditions. We began by assessing evoked local field potentials (LFPs) across channels (Fig. 3a–d). As expected, conventional surface illumination elicited the largest deflection in superficial layers (Fig. 3a). For stimulation with the  $\mu$ LED probe, we observed a different depth profile of LFPs, with larger deflection at deeper channels corresponding to deeper  $\mu$ LED stimulation (Fig. 3d).

We also computed the current source density (CSD, Fig. 3e–h) to determine the net extracellular current flow into and out of neocortical circuits as a function of distance<sup>33</sup>. This reinforces the differences between the two stimulation paradigms, with surface illumination inducing the largest current sink superficially and the  $\mu$ LED probe creating distinct spatiotemporal patterns of activation dependant on stimulus locations. To quantify these activation patterns on a single trial basis, first we reduced the data dimensionality by applying a principle component analysis (PCA, Fig. 3m), with the first three principle components explaining 94% of the variance. Importantly, these CSD depth profiles showed clear clusters depending on stimulus conditions, indicating different patterns of activity. We then classified each activation pattern under the three  $\mu$ LED stimulation conditions applying a linear classifier with ten-fold cross validation (Fig. 3n). As irradiance of  $\mu$ LED stimulation increased,

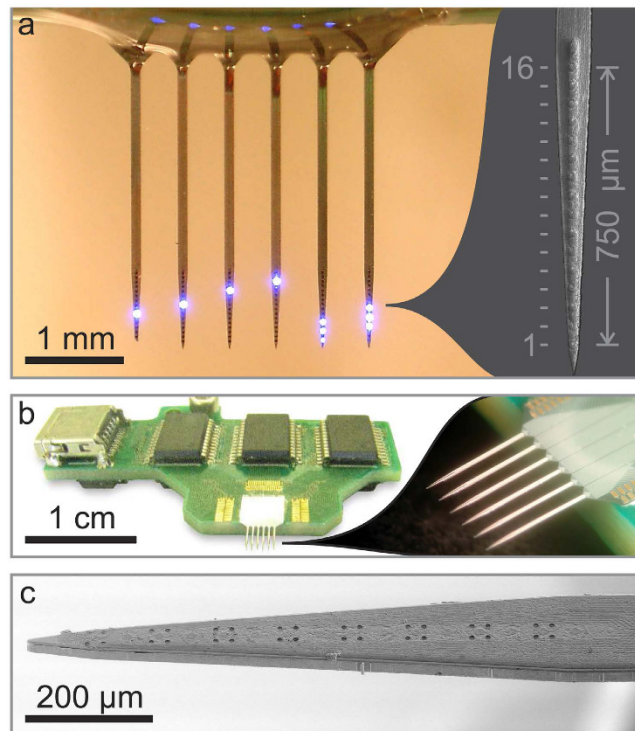


**Figure 4. Scalability of  $\mu$ LED neural probes.** (a) 6-shank  $\mu$ LED probe with 16  $\mu$ LEDs per shank, giving 96 individually addressable stimulation sites, left: patterns of activity can easily be created across the multi-shank probe, right: a scanning electron micrograph (SEM) of one of the shanks. (b) The probe system running from a USB interface that connects to a small PCB and offers electronic control over the 96  $\mu$ LEDs. (c) SEM of an integrated probe showing how microelectrodes can be incorporated into the  $\mu$ LED device to allow two-way communication with neural circuits.

the classification rate significantly improved from a chance level of 33%. This indicates that the clusters separate in PC-space, i.e. the induced CSD depth profiles become more distinctive.

We applied the same procedure in control animals without Chr2 expression (Ai32 mice,  $n = 3$ ), and confirmed the classification rate remained around the chance level. The significant difference ( $F_{1,7} = 75.69$ ,  $p < 0.0001$ , two-way ANOVA) between induced neural patterns in the control and Chr2 expressing mice demonstrates that our observations are due to Chr2 activation, rather than effects from localised light stimulation alone. Finally, we confirmed our observations based on multi-unit activities (MUAs) across channels (Fig. 3i–l). Depending on stimulus conditions, the location of peak activity and activity propagation patterns differed. Classification performance was qualitatively similar to that with CSD and LFP (Supplementary Figure S7). Thus, using our  $\mu$ LED probe even without a complex genetic approach, we could induce various spatiotemporal patterns of neural population activity *in vivo*.

To assess the invasiveness under our acute conditions, we used histological techniques (Supplementary Figure S8). While the track of the probe was often visible, we observed less than 100  $\mu$ m tissue damage by propidium iodide (PI) staining. This result is comparable with invasiveness of commonly used silicon-based multi-site electrodes, where the maximum thickness of commercially available probes is 50  $\mu$ m.

## Discussion

Microstimulation of neural populations has been a tremendously influential approach for investigating causal links between neural activity and behaviour. Our device offers a powerful tool to optogenetically stimulate the brain in a depth-dependent and cell-type specific manner. Although electrophysiological and optical recording of neural population activity has been performed in many brain areas and species with cellular resolution (even in freely behaving conditions), technologies for neural control still remain in their infancy. An important goal in this field is to develop technologies to deliver light in large volumes of biological tissue with high spatiotemporal resolution. Our novel device can overcome several technical challenges toward this end. Firstly, it can deliver light even in deep brain regions with micro-millimetre resolution. Since silicon-based electrodes can be implanted in the brain chronically for months, it will be interesting to investigate long-lasting effects of our device in freely behaving animals in the future. As the design is similar to silicon-based multisite electrodes, which have been used over the past decades<sup>34–38</sup>, our device enables us to perform a wide range of experiments with respect to optogenetic microstimulation.

Secondly, the device is scalable due to integration of light sources on the probe and the adoption of wafer-scale silicon microfabrication. Once microfabricated, the probes are easy to integrate into conventional biology labs with minimal costs. To further demonstrate this advantage we have produced a six-shank probe with 96  $\mu$ LEDs,

that can be controlled by off-the-shelf integrated circuits (Fig. 4 and Supplementary Figure S6b). Integration of electrode sites on the same device will allow more localized stimulation/recording of circuit responses and the integration of control electronics on-chip opens the door to very high-density devices. Indeed, Wu *et al.* recently demonstrated this capability<sup>21</sup>. Although their device contains 3  $\mu$ LEDs per shank, in the present study we demonstrated the scalability of this approach with having 16  $\mu$ LEDs and tested the probe to activate neurons across layers of the neocortex. As shown in Supplementary Figure S5, there is an interesting relationship between the size and pitch of  $\mu$ LEDs and achievable spatial resolution, suggesting design parameters for future probes. For example, although the smaller  $\mu$ LEDs provide increased spatial resolution, this links to the depth penetration of the light and at a certain intensity larger  $\mu$ LEDs offer a resolution similar to that of the smaller ones. This suggests that biological questions and constraints may define technological limits (such as the density and size of  $\mu$ LEDs). On the other hand, probes that include multi-colour stimulation, integrate wireless power and data transfer<sup>17</sup> and provide a three-dimensional distribution of light sources<sup>16</sup> will enable novel experiments to be conducted and are developments that can be integrated with the probes shown here.

One drawback of our approach is the inefficiency of electrical current conversion to light, meaning that heat is generated at the  $\mu$ LED surface. This is particularly relevant as we are directly inserting a probe into the tissue, positioning the light source next to the neurons and opening up the possibility that the temperature change itself modulates biological function. In this study we used light pulses of 50 ms duration, at a repetition rate of 2.8 Hz and an irradiance of up to 150 mW/mm<sup>2</sup>. According to our prediction (Fig. 1k) these parameters lead to an average temperature increase of ~0.5 °C. Although the peak temperature increase is ~2–4 °C at the  $\mu$ LED surface at the end of each pulse, this drops off quickly in time and space, with 50 ms pulses taking ~30 ms to cool below 0.5 °C (Fig. 1h,i). At the same time, neurons that are ~70  $\mu$ m away from the  $\mu$ LED never get exposed to these temperatures (Fig. 1j). Indeed we did not observe any significant effect of  $\mu$ LED stimulation without expressing ChR2 (Fig. 3n). Thermal restrictions can be eased further by employing other opsins<sup>39,40</sup>, which are more sensitive than commonly used ChR2 and allow activation with irradiances that are an order of magnitude lower. This means that the peak irradiances needed to excite a certain volume also drop by an order of magnitude. So, to replicate the results here, we would require only 15 mW/mm<sup>2</sup> peak (cf. 150 mW/mm<sup>2</sup>) to excite the same volume and the resulting reduction in electrical power means almost any combination of pulse duration and duty cycle keeps the peak temperature below 0.5 °C. These opsins will open up new possibilities for complex, massively parallel optogenetic stimulation patterns using multiple  $\mu$ LEDs.

Although modelling indicates that the probe is capable of high-density optical stimulation at a resolution of 10 s of microns (Supplementary Figure S5), due to the lack of integrated recording sites in the probe tested *in vivo*, the present study only demonstrated depth-specific neural activations at a resolution of 100 s of microns. As Wu *et al.*<sup>21</sup> demonstrated, it would be interesting to further validate our technology to achieve neural control at 10 s of microns resolution. Our probe will also allow coverage of a larger volume of the brain tissue due to the increased number of channels. Another limitation of the current study is that the probe has been tested in an acute preparation only (several hours). Therefore, it is uncertain to what extent the probe may introduce foreign body tissue reaction to cause further invasiveness. In addition, the effect of long-term optical illuminations on the tissue will need to be assessed histologically.

However, despite these limitations there are several immediate applications of our probe as demonstrated here. One particularly useful application is when optical illumination is required at higher spatial resolution in a deep brain area compared to conventional optical fibre stimulations. An ideal target is a cell class distributed across functionally distinct sub-regions in a small volume of brain tissue, such as cortical GABAergic neurons. This application offers an opportunity to perform *in vivo* activation of a particular genetically defined cell-type in a depth dependent manner at a resolution of at least 100 s of microns. Activating a sub-cellular component of a particular cell-type (such as the apical dendrites of pyramidal cells or axonal terminals in different input layers in a single brain area) is an interesting application (however, this is not simple - see Wu *et al.*<sup>21</sup>). It is also feasible to activate a specific group of neurons within a topographically organized brain area, such as the tonotopic map in the auditory system.

Another application is one where various spatiotemporal patterns of neural activity need to be induced without employing complex genetic manipulations. While we have used transgenic mice to demonstrate the technology, in many species it is a challenge to express opsins in a cell-type-specific manner. Our probe offers the opportunity to perform new types of optogenetic experiments with a conventional molecular biological approach. In addition, a caveat of conventional optogenetic activations is to generate unnatural, excessive synchronous activation in a large number of neurons although spatiotemporally organized neural population activity is a fundamental ingredient of neural coding<sup>37,41–43</sup>. The further development of our probe can open up possibilities to artificially mimic the dynamic nature of neural population activity at high spatiotemporal resolution *in vivo*. This will enhance efforts to understand neural function and to develop new strategies to treat brain disorders.

## Methods

**Semiconductor fabrication.** In order to produce minimally invasive devices, we fabricated Si-based  $\mu$ LED probes (Fig. 1) starting from a 6-inch GaN-on-Si wafer material (Plessey Semiconductors Ltd, UK). The  $\mu$ LED structures were grown on Si(111) wafers by MOVPE (metalorganic vapour phase epitaxy). Further details of growth and the epitaxial layer sequence are available elsewhere<sup>44</sup>. In brief, the epitaxial structures consist of an AlN nucleation layer, an AlGaN strain management layer, and a Si-doped GaN layer, followed by InGaN/GaN multiple quantum wells (MQWs), an AlGaN current blocking layer, and a p-type GaN layer.

**Probe fabrication.** The fabrication process was as follows: A thin layer of Ni/Au (10 nm:20 nm) was electron-beam evaporated onto the surface of the wafer and forms a current spreading contact to the p-type GaN. This metal layer was then photolithographically patterned and reactive-ion etched, followed by an inductively

coupled plasma (ICP) etch of the p-type GaN that exposed the n-type layer. This creates isolated 25  $\mu\text{m}$ -diameter mesa-structures that form the  $\mu\text{LEDs}$ . The wafer was then thermally annealed to ensure good electrical contact between the Ni/Au layer and the p-type GaN. A Ti/Al metal layer was sputter-deposited to serve as a contact to the n-GaN, covering the whole sample except the  $\mu\text{LED}$  sites. After this, an insulating bilayer of  $\text{SiO}_2$  was deposited using PECVD and selectively etched on the  $\mu\text{LEDs}$  to make contact with the current spreading layer. A Ti/Al metal stack was deposited to create the sixteen tracks for the  $\mu\text{LEDs}$  and ICP etched, followed by the deposition of another  $\text{SiO}_2$  bilayer. Contact pad vias were etched and Ti/Au contact pads were deposited to facilitate wire bonding. Trenches around each device were created by deep reactive ion etching and defined the final probe shape. The devices were thinned from the backside to a final thickness of 30  $\mu\text{m}$  (DISCO HI-TEC EUROPE GmbH, Germany), which also singulates each probe. Probes were then separated from the frame and die and wire bonded to a custom-designed PCB. The wire bonds were potted using a UV-curable epoxy. A  $\sim 6 \mu\text{m}$  thick layer of parylene C was conformally deposited on the probe for insulation and to improve biocompatibility (cf. Supplementary Figure S1). This process has now been developed to the point where we are achieving yields of 75% (in terms of individually addressable  $\mu\text{LEDs}$ ) with electrical shorts and breaks being the dominant sources of failure.

**Simulation of Light propagation.** Monte Carlo Simulations have been conducted to assess the expected light propagation in brain tissue. The  $\mu\text{LED}$  was treated as a Lambertian source. The material parameters of the brain tissue were assumed to be the following<sup>45</sup>: absorption coefficient  $\mu_a = 0.7 \text{ cm}^{-1}$ , scattering coefficient  $\mu_s = 117 \text{ cm}^{-1}$ , anisotropy factor  $g = 0.88$ .

**Simulation of Heat dissipation.** Simulations of heat transfer in the  $\mu\text{LED}$  probe and surrounding medium were conducted using COMSOL Multiphysics<sup>®</sup>. The probe was included in the model with its original geometry (cf. Supplementary Figure S3). To make use of its symmetry, only one half was modelled. The material was assumed to be pure silicon. The  $\mu\text{LEDs}$  were modelled as half cylinders with 1  $\mu\text{m}$  height and 25  $\mu\text{m}$  diameter. The whole probe was surrounded with a 6  $\mu\text{m}$  thin layer of parylene C. A half cuboid surrounded the tip of the probe. The material was chosen to be either brain tissue or air, while the bonding area of the probe was always surrounded by a cuboid of air. The boundaries of the media were held at a constant temperature  $T_0$ . Heating of the probe was simulated using boundary heat sources at the  $\mu\text{LED}$ /parylene interface where the  $\mu\text{LED}$  was assumed to be perfectly inefficient (all input electrical power converted to heat, wall plug efficiency is  $\sim 1\%$ ). The simulated electrical power of the boundary heat source was extracted from a typical IV-curve ( $P_{el} = V \cdot I$ ). The material parameters in the simulation were assumed to be the following: brain<sup>46</sup> – density  $\rho = 1040 \text{ kg m}^{-3}$ , heat capacity  $C_p = 3650 \text{ J kg}^{-1} \text{ K}^{-1}$ , thermal conductivity  $k = 0.527 \text{ W m}^{-1} \text{ K}^{-1}$ , silicon – density  $\rho = 2329 \text{ kg m}^{-3}$ , heat capacity  $C_p = 700 \text{ J kg}^{-1} \text{ K}^{-1}$ , thermal conductivity  $k = 130 \text{ W m}^{-1} \text{ K}^{-1}$ , parylene C – density  $\rho = 1289 \text{ kg m}^{-3}$ , heat capacity  $C_p = 712 \text{ J kg}^{-1} \text{ K}^{-1}$ , thermal conductivity  $k = 0.084 \text{ W m}^{-1} \text{ K}^{-1}$ , air – (temperature-dependent model from COMSOL).

**Animals.** All animal experiments were performed in accordance with the UK Animals (Scientific Procedures) Act of 1986 Home Office regulations and approved by the Home Office and University's Ethical Committee (PPL 60/4217). Emx1-IRES-Cre (Jax#005628)<sup>47</sup>, PV-IRES-Cre (Jax#008069) and Ai32 (Jax#012569)<sup>48</sup> were used to express Chr2(H134R). Seven Emx1-IRES-Cre::Ai32 (male, 10–20 week old), one PV-IRES-Cre::Ai32 (male, 26 week old), and three Ai32 mice (female, 14–32 week old) were used in this study. Two of Emx1-IRES-Cre::Ai32 mice were used for the mechanical testing (Supplementary Figure S8).

**Optoelectrophysiological experiments.** All experiments were performed under urethane anaesthesia. After animals were anesthetized with 1.5 g/kg urethane, they were placed in a stereotaxic frame (Narishige) and body temperature was retained at 37 °C using a feedback temperature controller (40-90-8C, FHC or 50-7221-F, Harvard Bioscience, Inc.). After incision, the bone above the right sensorimotor cortices (0–2 mm posterior from the bregma, 0–2 mm lateral from the midline) was removed and the cavity was filled with warm saline during the entire recording session. The  $\mu\text{LED}$  probe was slowly inserted into the cortex with a 20° angle and penetrated 1.1–1.5 mm depending on probes. A 32-channel silicon-based optrode (A1  $\times$  32-10 mm-50-177-A320A, NeuroNexus Technologies) was inserted slowly ( $\sim 2 \mu\text{m/s}$ ) and penetrated 1.0–1.1 mm with a motorized manipulator (DMA-1511, Narishige). The distance between the  $\mu\text{LED}$  probe and optrode was 400  $\mu\text{m}$  at the cortical surface. For histological verification of tracks, the rear of both probes was painted with DiI (D-282,  $\sim 10\%$  in ethanol, Life Technologies)<sup>34,37</sup>.

For electrophysiological recording, broadband signals were amplified (HST/32V-G20 and PBX3, Plexon or RHD2132, Intan Technologies, LLC) relative to a cerebellar bone screw and were digitized at 20 kHz (PXI, National Instruments or RHD2132 and RHD2000, Intan Technologies, LLC). Once both probes were inserted into the target depth, recording sessions were initiated. Each recording session typically consisted of a non-stimulation period (at least 2 min), the intensity testing period and another non-stimulation period (up to 2 min). The non-stimulation period was for assessing spontaneous activity. In the intensity testing period, optical stimulation from an optic fibre of the optrode (86.6  $\text{mW/mm}^2$ ) was applied at the beginning, followed by  $\mu\text{LED}$  stimulation with varied irradiances (0.1–150  $\text{mW/mm}^2$ ) and then the optic fibre stimulation. Each optical stimulation consisted of 50 ms pulses at 2.8 Hz repetition rate (300 ms interval) with 100 repetitions. In some of experiments, we also took additional optical stimulation regimes, such as optical stimulation with varied pulse widths and repetition rates. In the present study, we only report results from the intensity testing.

**Signal processing.** LFPs were extracted from the broadband signal after low pass ( $< 800 \text{ Hz}$ ) filtering and re-sampling at 1 kHz across channels. All spike detection and sorting took place offline. For this process, freely available software (KlustaSuite, <https://github.com/klusta-team>) was used. In the experiment in the

PV-IRES-Cre::Ai32 mouse, we analysed only single units which fulfilled the following two conditions: 1) with isolation distance<sup>49</sup> values  $\geq 20$  and 2) with response probability values  $> 0.7$  to optical stimulation from the cortical surface. In the experiments in Emx1-IRES-Cre::Ai32 mice, due to excessive spike overlap during optical stimulation, we detected spike events for each channel using the KlustaSuite and treated spike events as multiple unit activity (MUA). All spike train and LFP analysis was performed using Matlab (Mathworks).

**Depth estimation of single units.** As described elsewhere<sup>37,50</sup>, the depth of spike-sorted units was estimated from the stereotaxically measured depth of the electrode tip and spike waveform profiles. Somatic location was estimated as the recording site with mean waveform of maximum peak-to-trough amplitude.

**Current source density analysis.** CSD depth profiles were generated from depth profiles of average LFPs using previously described methods<sup>33,37</sup>. First, we duplicated LFPs corresponding to the uppermost and lowermost channels. Second, LFPs were smoothed across spatially adjacent channels to reduce high spatial-frequency noise components:

$$\bar{\varphi}(r) = \frac{1}{4}(\varphi(r+h) + 2\varphi(r) + \varphi(r-h)) \quad (1)$$

where  $\varphi(r)$  is the LFP at depth  $r$ , and  $h$  is the sampling interval (50  $\mu\text{m}$ ). Next, we calculated the second derivative:

$$D = \frac{1}{h^2}(\bar{\varphi}(r+h) - 2\bar{\varphi}(r) + \bar{\varphi}(r-h)) \quad (2)$$

For visualization purposes, data were linearly interpolated and plotted as pseudocolour images, with red (current sink) and blue (current source).

**Classification analysis.** A principal component analysis (PCA) with singular value decomposition was applied to reduce the dimensionality of CSD depth profiles on a single trial basis. Signals from the bottom 17 or 19 channels were used. To eliminate optical and electrical artefacts, a time window from 4–49 ms from the onset of optical stimulation was taken. Each CSD map was treated as a single vector and then a PCA (Matlab *pca* function) was applied.

For classification analysis, 10-fold cross validation for linear discriminant analysis (Matlab *crossval* function) was performed with the first three PCs mentioned above, then the overall successful classification rate across all tests was computed.

**Statistical analysis.** Data were presented as mean  $\pm$  SEM. For multiple comparisons, two-way ANOVA was performed, followed by post-hoc Tukey's honest significant difference (HSD) test. All statistical analyses were conducted using Matlab.

**Data Availability.** The raw data recorded for this article is publicly available and can be found at: <http://dx.doi.org/10.15129/a8b7f487-3903-4bee-a2a9-71195599e12d>

## References

- Zemelman, B. V., Lee, G. A., Ng, M. & Miesenböck, G. Selective Photostimulation of Genetically ChARGed Neurons. *Neuron* **33**, 15–22 (2002).
- Nagel, G. *et al.* Channelrhodopsin-2, a directly light-gated cation-selective membrane channel. *Proc. Natl. Acad. Sci.* **100**, 13940–13945 (2003).
- Boyden, E. S., Zhang, F., Bamberg, E., Nagel, G. & Deisseroth, K. Millisecond-timescale, genetically targeted optical control of neural activity. *Nat. Neurosci.* **8**, 1263–1268 (2005).
- Yizhar, O., Fenno, L. E., Davidson, T. J., Mogri, M. & Deisseroth, K. Optogenetics in neural systems. *Neuron* **71**, 9–34 (2011).
- Häusser, M. Optogenetics: the age of light. *Nat. Methods* **11**, 1012–1014 (2014).
- Miesenböck, G. Optogenetic control of cells and circuits. *Annu. Rev. Cell Dev. Biol.* **27**, 731–758 (2011).
- Adamantidis, A. R., Zhang, F., Aravanis, A. M., Deisseroth, K. & de Lecea, L. Neural substrates of awakening probed with optogenetic control of hypocretin neurons. *Nature* **450**, 420–424 (2007).
- Aravanis, A. M. *et al.* An optical neural interface: *in vivo* control of rodent motor cortex with integrated fiberoptic and optogenetic technology. *J. Neural Eng.* **4**, S143 (2007).
- Rickgauer, J. P., Deisseroth, K. & Tank, D. W. Simultaneous cellular-resolution optical perturbation and imaging of place cell firing fields. *Nat. Neurosci.* **17**, 1816–1824 (2014).
- Szabo, V., Ventalon, C., De Sars, V., Bradley, J. & Emiliani, V. Spatially Selective Holographic Photoactivation and Functional Fluorescence Imaging in Freely Behaving Mice with a Fiberscope. *Neuron* **84**, 1157–1169 (2014).
- Packer, A. M., Russell, L. E., Dalglish, H. W. P. & Häusser, M. Simultaneous all-optical manipulation and recording of neural circuit activity with cellular resolution *in vivo*. *Nat. Methods* **12**, 140–146 (2015).
- Rickgauer, J. P. & Tank, D. W. Two-photon excitation of channelrhodopsin-2 at saturation. *Proc. Natl. Acad. Sci.* **106**, 15025–15030 (2009).
- Pisanello, F. *et al.* Multipoint-Emitting Optical Fibers for Spatially Addressable *in Vivo* Optogenetics. *Neuron* **82**, 1245–1254 (2014).
- Lee, J., Ozden, I., Song, Y.-K. & Nurmikko, A. V. Transparent intracortical microprobe array for simultaneous spatiotemporal optical stimulation and multichannel electrical recording. *Nat. Methods* **12**, 1157–1162 (2015).
- Wu, F. *et al.* An implantable neural probe with monolithically integrated dielectric waveguide and recording electrodes for optogenetics applications. *J. Neural Eng.* **10**, 056012 (2013).
- Zorzos, A. N., Scholvin, J., Boyden, E. S. & Fonstad, C. G. Three-dimensional multiwaveguide probe array for light delivery to distributed brain circuits. *Opt. Lett.* **37**, 4841–4843 (2012).
- Kim, T. *et al.* Injectable, Cellular-Scale Optoelectronics with Applications for Wireless Optogenetics. *Science* **340**, 211–216 (2013).
- McAlinden, N. *et al.* Thermal and optical characterization of micro-LED probes for *in vivo* optogenetic neural stimulation. *Opt. Lett.* **38**, 992–994 (2013).
- Moser, T. Optogenetic stimulation of the auditory pathway for research and future prosthetics. *Curr. Opin. Neurobiol.* **34**, 29–36 (2015).

20. McAlinden, N., Gu, E., Dawson, M. D., Sakata, S. & Mathieson, K. Optogenetic activation of neocortical neurons *in vivo* with a sapphire-based micro-scale LED probe. *Front. Neural Circuits* **9**, (2015).
21. Wu, F. *et al.* Monolithically Integrated  $\mu$ LEDs on Silicon Neural Probes for High-Resolution Optogenetic Studies in Behaving Animals. *Neuron* **88**, 1136–1148 (2015).
22. Schüz, A. & Palm, G. Density of neurons and synapses in the cerebral cortex of the mouse. *J. Comp. Neurol.* **286**, 442–455 (1989).
23. Koch, C. *Biophysics of computation information processing in single neurons*. (Oxford University Press, 1999).
24. Elwassif, M. M., Kong, Q., Vazquez, M. & Bikson, M. Bio-Heat Transfer Model of Deep Brain Stimulation Induced Temperature changes. In *28th Annual International Conference of the IEEE Engineering in Medicine and Biology Society, 2006. EMBS '06* 3580–3583 (2006).
25. Andersen, P. & Moser, E. I. Brain temperature and hippocampal function. *Hippocampus* **5**, 491–498 (1995).
26. Szentágothai, J. In *Reviews of Physiology, Biochemistry and Pharmacology*, Volume 98 11–61 (Springer Berlin Heidelberg, 1983).
27. Xu, H., Jeong, H.-Y., Tremblay, R. & Rudy, B. Neocortical Somatostatin-Expressing GABAergic Interneurons Disinhibit the Thalamorecipient Layer 4. *Neuron* **77**, 155–167 (2013).
28. Bortone, D. S., Olsen, S. R. & Scanziani, M. Translaminar Inhibitory Cells Recruited by Layer 6 Corticothalamic Neurons Suppress Visual Cortex. *Neuron* **82**, 474–485 (2014).
29. Harris, K. D. & Shepherd, G. M. G. The neocortical circuit: themes and variations. *Nat. Neurosci.* **18**, 170–181 (2015).
30. Ascoli, G. A. *et al.* Petilla terminology: nomenclature of features of GABAergic interneurons of the cerebral cortex. *Nat. Rev. Neurosci.* **9**, 557–568 (2008).
31. Markram, H. *et al.* Interneurons of the neocortical inhibitory system. *Nat. Rev. Neurosci.* **5**, 793–807 (2004).
32. Rudy, B., Fishell, G., Lee, S. & Hjerling-Leffler, J. Three groups of interneurons account for nearly 100% of neocortical GABAergic neurons. *Dev. Neurobiol.* **71**, 45–61 (2011).
33. Freeman, J. A. & Nicholson, C. Experimental optimization of current source-density technique for anuran cerebellum. *J. Neurophysiol.* **38**, 369–382 (1975).
34. Blanche, T. J., Spacek, M. A., Hetke, J. F. & Swindale, N. V. Polytrodes: High-Density Silicon Electrode Arrays for Large-Scale Multiunit Recording. *J. Neurophysiol.* **93**, 2987–3000 (2005).
35. Berényi, A. *et al.* Large-scale, high-density (up to 512 channels) recording of local circuits in behaving animals. *J. Neurophysiol.* **111**, 1132–1149 (2014).
36. Csicsvari, J. *et al.* Massively Parallel Recording of Unit and Local Field Potentials With Silicon-Based Electrodes. *J. Neurophysiol.* **90**, 1314–1323 (2003).
37. Sakata, S. & Harris, K. D. Laminar Structure of Spontaneous and Sensory-Evoked Population Activity in Auditory Cortex. *Neuron* **64**, 404–418 (2009).
38. Du, J. *et al.* High-Resolution Three-Dimensional Extracellular Recording of Neuronal Activity With Microfabricated Electrode Arrays. *J. Neurophysiol.* **101**, 1671–1678 (2009).
39. Klapoetke, N. C. *et al.* Independent optical excitation of distinct neural populations. *Nat. Methods* **11**, 338–346 (2014).
40. Govorunova, E. G., Sineshchekov, O. A., Janz, R., Liu, X. & Spudich, J. L. Natural light-gated anion channels: A family of microbial rhodopsins for advanced optogenetics. *Science* **349**, 647–650 (2015).
41. Yuste, R. From the neuron doctrine to neural networks. *Nat. Rev. Neurosci.* **16**, 487–497 (2015).
42. Buzsáki, G. Neural Syntax: Cell Assemblies, Synapsesembles, and Readers. *Neuron* **68**, 362–385 (2010).
43. Hebb, D. O. *The Organization of Behavior*. (John Wiley & Sons Inc, 1949).
44. Zhu, D. *et al.* High-efficiency InGaN/GaN quantum well structures on large area silicon substrates. *Phys. Status Solidi A* **209**, 13–16 (2012).
45. Yaroslavsky, A. N. *et al.* Optical properties of selected native and coagulated human brain tissues *in vitro* in the visible and near infrared spectral range. *Phys. Med. Biol.* **47**, 2059 (2002).
46. Stujenske, J. M., Spellman, T. & Gordon, J. A. Modeling the Spatiotemporal Dynamics of Light and Heat Propagation for *in Vivo* Optogenetics. *Cell Rep.* **12**, 525–534 (2015).
47. Gorski, J. A. *et al.* Cortical Excitatory Neurons and Glia, But Not GABAergic Neurons, Are Produced in the Emx1-Expressing Lineage. *J. Neurosci.* **22**, 6309–6314 (2002).
48. Madisen, L. *et al.* A toolbox of Cre-dependent optogenetic transgenic mice for light-induced activation and silencing. *Nat. Neurosci.* **15**, 793–802 (2012).
49. Schmitzer-Torbert, N., Jackson, J., Henze, D., Harris, K. & Redish, A. D. Quantitative measures of cluster quality for use in extracellular recordings. *Neuroscience* **131**, 1–11 (2005).
50. Sakata, S. & Harris, K. D. Laminar-dependent effects of cortical state on auditory cortical spontaneous activity. *Front. Neural Circuits* **6**, 109 (2012).

## Acknowledgements

This work was supported by BBSRC (BB/K016830/1) to SS, EPSRC (EP/I029141/1) to MDD, a pilot project through EP/G042446/1 to KM and a JSPS postdoctoral fellowship for research abroad to TT. We thank Prof. Sir C. Humphreys, Drs. D. Wallis and D. Zhu of Plessey Semiconductors Ltd. and Cambridge University for supplying wafers of GaN-on-Si material and Drs. D.E. Gunning, I.M. Watson and E. Gu for advice on microfabrication.

## Author Contributions

K.M., S.S., M.D.D. and R.S. conceived the device and study presented. R.S. designed and fabricated the neural probes under guidance of K.M. and R.S. modelled the device and alongside N.M. characterized performance. S.S. led the physiological testing and data analysis, which T.T. and S.S. conducted. T.T. performed histological analysis. R.S. is first author of the manuscript, which was edited by K.M. and S.S. and who share senior authorship.

## Additional Information

**Supplementary information** accompanies this paper at <http://www.nature.com/srep>

**Competing financial interests:** The authors declare no competing financial interests.

**How to cite this article:** Scharf, R. *et al.* Depth-specific optogenetic control *in vivo* with a scalable, high-density  $\mu$ LED neural probe. *Sci. Rep.* **6**, 28381; doi: 10.1038/srep28381 (2016).



This work is licensed under a Creative Commons Attribution 4.0 International License. The images or other third party material in this article are included in the article's Creative Commons license, unless indicated otherwise in the credit line; if the material is not included under the Creative Commons license, users will need to obtain permission from the license holder to reproduce the material. To view a copy of this license, visit <http://creativecommons.org/licenses/by/4.0/>